Materials Advances

ROYAL SOCIETY OF CHEMISTRY

PAPER

View Article Online
View Journal | View Issue

Cite this: *Mater. Adv.*, 2026, 7, 2300

A novel copper formate-based framework $RbCu(HCO_2)_2Cl$: synthesis, crystal structure, thermal, vibrational and magnetic properties and antibacterial activity

Asmae Ben Abdelhadi,[ab] Safaa Hidaoui,[a] Rachid Ouarsal,[a] Morgane Poupon,[c] Michal Dusek,[c] María de los Llanos Palop Herreros,[d] Marco Antonio López de la Torre,[e] Luis Lezama,[f] Brahim El Bali,[a] Mohammed Lachkar *[a] and Abderrazzak Douhal *[b]

In this contribution, we report on the synthesis and characterization of a novel biologically active Cu(II)-based paddle-wheel (PW) metal–organic framework (MOF), $RbCu(HCO_2)_2Cl$ (**1**). Single-crystal X-ray diffraction results confirmed a monoclinic unit cell with space group $P2_1/n$ and the Rb^+ cation as a counter-balanced ion located in the cavities of the framework of the dinuclear copper–copper dimer formed by a PW-arrangement of formate anions in the *syn–syn* configuration. Each Cu(II) atom has a square-pyramidal environment with a Cu···Cu intramolecular distance of 2.7070 (7) Å. The IR spectrum confirms the existence of the formate anion (HCO_2^-). Magnetic susceptibility experiments, performed from 5 to 300 K, revealed a strong antiferromagnetic coupling ($J = -531\ cm^{-1}$) between the two Cu^{2+} ions linked by four formate groups. The powder EPR spectra show the typical lines of the triplet state ($S = 1$) with significant zero-field splitting, attributed to Cu^{2+}–Cu^{2+} dimers. *In vitro* antibacterial activity was evaluated against two Gram-positive bacteria (*Staphylococcus aureus* CECT 86 and *Listeria monocytogenes* CECT 4031) and two Gram-negative bacteria (*Escherichia coli* CECT 99 and *Klebsiella pneumoniae* CECT 143[T]). The studies revealed that MOF **1** exhibits both bacteriostatic and bactericidal activity against all the microorganisms analyzed, making it a potential candidate for treating bacterial infections. The obtained findings provide more insight into the interesting properties of Cu-based frameworks and antibacterial activity.

Received 13th September 2025,
Accepted 14th December 2025

DOI: 10.1039/d5ma01055a

rsc.li/materials-advances

1. Introduction

Metal–organic frameworks (MOFs) are an important class of hybrid crystalline materials made of metal centres and organic linkers. They offer adjustable structures, high porosity, and multifunctionality. Their structural flexibility and chemical diversity have enabled many applications, including catalysis, gas storage, sensing, magnetism and increasingly, biological uses.[1–3] Recently, research has focused on exploring MOFs with a binuclear paddle wheel (PW) topology. Their outstanding porosity, adjustable design and their unique physicochemical properties make them promising for various applications, such as biologically active agents, electrochemical processes, ferroelectric and dielectric materials, magnetism, catalysis, supramolecular assemblies, and molecular magnetic devices.[4–8] Among various metal ions used in PW-based MOF chemistry, copper is one of the most widely employed metal centres for forming paddle-wheel structures, and it is a significant transition metal in biology and coordination chemistry.[9–13] Copper is

[a] *Engineering Laboratory of Organometallic, Molecular Materials, and Environment (LIMOME), Faculty of Sciences, Sidi Mohamed Ben Abdellah University, 30000 Fez, Morocco. E-mail: mohammed.lachkar@usmba.ac.ma*
[b] *Departamento de Química Física, Facultad de Ciencias Ambientales y Bioquímica, e INAMOL, Campus Tecnológico de Toledo, Universidad de Castilla-La Mancha (UCLM), Avenida Carlos III, S.N., 45071 Toledo, Spain. E-mail: Abderrazzak.Douhal@uclm.es*
[c] *Institute of Physics of the Czech Academy of Sciences, Na Slovance 2, 8, Praha 182 21, Czech Republic*
[d] *Departamento de Química Analítica y Tecnología de los Alimentos, Facultad de Ciencias Ambientales y Bioquímica, Universidad de Castilla-La Mancha, (UCLM), Avenida Carlos III, S.N., 45071 Toledo, Spain*
[e] *Departamento de Física, Facultad de Ciencias Ambientales y Bioquímica, e INAMOL, Universidad de Castilla-La Mancha, Avenida Carlos III, S.N., 45071 Toledo, Spain*
[f] *Departamento de Química Orgánica e Inorgánica, Facultad de Ciencia y Tecnología, Universidad del País Vasco, UPV/EHU, B° Sarriena s/n, 48940 Leioa, Spain*

an essential trace element in the human body. In addition, it plays crucial roles in many biological processes and enzyme regulation, as well as in the structural and functional enhancement of proteins; it also exhibits intrinsic antimicrobial and redox activity. Consequently, the combination of biologically relevant copper centres with the structural robustness of the PW motif offers a promising platform for the design of functional materials with enhanced biological activity.[14,15] Notably, numerous studies have shown that Cu–PW MOFs are being extensively explored for biological applications. These include antibacterial, anticancer, antifungal, antimicrobial, and antiviral activities, which arise from the unique coordination sphere around central Cu(II) cations, their ability to catalyze the generation of reactive oxygen species (ROS), disrupt membrane integrity, interact with nucleic acids, and inhibit key microbial enzymes.[14,16,17] These multifunctional properties make Cu(II) MOFs biologically more relevant and functional than other compounds. The higher biological activity of Cu(II)-based MOFs is significantly influenced by the nature of the ligands used. In particular, N- and O-donor ligands represent a promising class of candidates in the development of new Cu(II)-based antimicrobial materials. These ligands often coordinate the copper metal through different coordination geometries (four, five, or six), forming a stable chelating framework. This chelation process generally reduces the polarity of the copper center, increases the lipophilicity of the compound and thereby improves its ability to penetrate biological membranes, leading to enhanced biological activity.[16,18–20] In addition to that, Cu PW-based MOFs have gained significant interest, owing to their magnetic behaviour, facilitated by the rather short formate anion HCO_2^-, which allows strong magnetic coupling between the Cu(II) centers.[21,22] In general, a Cu(II)-based compound contains an unpaired d^9 electron configuration that gives its paramagnetic properties. Additionally, it has been reported that the coupling of the d^9 unpaired electrons between the Cu(II) centers can result in a triplet (high spin) or a singlet (low spin) ground state or other magnetic properties such as ferromagnetic (FM) and antiferromagnetic (AFM) behavior, respectively. This depends on the types of coordination modes, metal geometry and environment.[23,24] In this context, the design and development of novel Cu-based PW frameworks, along with the investigation of their magnetic behaviour and the exploration of their biological activity remain an active and promising area of research for a better understanding of the structure–activity relationship.

Herein, we synthesized, fully characterized, examined the magnetic properties, and explored the biological activity of a novel Cu(II)-based MOF, $RbCu(HCO_2)_2Cl$ (**1**), containing the largest possible monoatomic A-site cations Rb^+. The Cu-based MOF was obtained by a slow diffusion method, with excellent reproducibility and was fully characterized by a combination of single crystal X-ray diffraction (SXRD), thermal stability, EPR and SQUID techniques. At 300 K, **1** crystallizes in the monoclinic system with space group $P2_1/n$, and its crystal structure features the well-known paddle-wheel motif typical of copper formates, $Cu_2(HCOO)_4$, with an intramolecular Cu···Cu distance of 2.7070(7) Å within the dinuclear unit. Magnetic susceptibility data, obtained from 5 to 300 K, revealed that **1** exhibits a strong antiferromagnetic coupling ($J = -531$ cm^{-1}) between the two Cu^{2+} ions linked by four formate groups, which form the Cu_2 paddle-wheel units that give rise to the anionic network in this compound. Furthermore, we also evaluated the *in vitro* antibacterial activity of MOF **1** against two Gram-positive bacteria, *S. aureus* CECT 86 and *L. monocytogenes* CECT 4031, and two Gram-negative bacteria, *E. coli* CECT 99 and *K. pneumoniae* CECT 143^T, using both the disc diffusion and the agar well diffusion methods.

2. Experimental section

2.1. Materials

All the chemicals are of reagent grade and were used as supplied. Copper(II) chloride tetrahydrate ($CuCl_2{\cdot}4H_2O$, 99.9%) and formic acid (HCOOH, 98%) were purchased from Fluka (Switzerland). Rubidium carbonate (Rb_2CO_3, 99.5%) was bought from Sigma-Aldrich (France) and anhydrous methanol (99.7%) was purchased from Panreac (Spain).

2.2. Synthesis

The green prismatic single crystals of **1** were obtained using a mild solution chemistry approach at ambient temperature using methanol as solvent, since it is widely known as a non-coordinating medium in synthesizing metal formate frameworks.[25] In a typical synthesis procedure, 10 mL of a methanolic solution containing 4 mmol of rubidium carbonate (0.92 g) and 80 mmol of formic acid (4 mL) were placed at the bottom of a glass tube. Upon this solution, 10 mL of a methanolic solution containing 2 mmol of $CuCl_2{\cdot}4H_2O$ (0.340 g) were carefully layered on top. The tube was sealed and undisturbed at room temperature for several days until green square-shaped crystals are formed. The crystals of **1** were subsequently isolated by filtration, washed three times with ethanol, and dried at room temperature for 24 h; the resulting crystals were quite stable (Fig. S1). HR-ESI-MS (negative mode) *m*/*z* calculated for $RbCuC_2H_2O_4Cl$: 274.50100; found: 273.94864.

2.3. Characterization and measurements

Single-crystal datasets were collected at 300 K, on a suitable green single crystal of **1** with dimensions 0.36 × 0.30 × 0.27 mm^3. Data collection was performed using Mo Kα radiation (λ = 0.71073 Å) from a classical sealed tube monochromated by graphite and collimated using a fibre-optics enhanced collimator. As a detector, we used a CCD Atlas S2. CrysAlis PRO software (CrysAlis PRO 1.171.41.117a, Rigaku Oxford Diffraction, 2021) was used to process the data and an empirical multiscan absorption correction was applied using spherical harmonics, implemented in the SCALE3 ABSPACK scaling algorithm. The structure was solved by charge flipping with the SUPERFLIP package[26] and refined against F^2 by using full-matrix least-squares method with the Jana2020 program package.[27] All non-hydrogen atoms were refined with anisotropic thermal displacement parameters. For all the hydrogen

atoms, we kept $U_{iso}(H)$ equal to $1.2U_{eq}(C/N)$. Visualization of the structure was made using the Diamond program.[28]

The details concerning the crystal data, data collection, and refinement are given in Table 1. At the same time, the refined atomic positions and displacement parameters are listed in Tables S1 and S2, respectively.

Mass spectrometry (MS) analyses. MS analyses were performed using a high-resolution Exactive Plus Orbitrap mass spectrometer (Thermo Scientific) equipped with an electrospray ionization (ESI) source.

Infrared spectroscopy measurements. The room-temperature infrared (IR) spectrum in the mid-IR (4000–400 cm^{-1}) range was measured with a Vertex 70 (Bruker) Fourier transform infrared spectrometer (FTIR) using the attenuated total reflectance (ATR) method. The spectral resolution was 4 cm^{-1}.

Thermogravimetric analysis (TGA) and differential thermal analysis (DTA). TGA–DTA analysis for the investigated compound was performed in the temperature range of 315 to 560 K using the LINSEIS TGA PT1600 apparatus. The sample weight was 3 mg. The heating speed rate was 10 K min^{-1} using an open platinum crucible under airflow.

EPR and magnetometry measurements. X-band EPR measurements were carried out on a Bruker ELEXSYS 500 spectrometer equipped with a super-high-Q resonator ER-4123-SHQ and a maximum available microwave power of 200 mW. Powder samples were placed in quartz tubes and the spectra were recorded at different temperatures between 4 and 300 K using standard Oxford Instruments low-temperature devices. The magnetic field was calibrated with an NMR probe and the frequency inside the cavity (~9.4 GHz) was determined with an integrated MW-frequency counter. For Q-band studies, the EPR spectra were recorded at room temperature on a Bruker EMX apparatus equipped with an ER-510-QT resonator. The frequency inside the cavity (~34 GHz) was determined with a Hewlett-Packard 5352B microwave frequency counter. The data were collected and processed using the Bruker Xepr suite. The temperature-dependent magnetic susceptibility measurements were performed between 5 and 300 K with an applied field of 1 kOe, using an MPMS3 SQUID magnetometer (Quantum Design). The magnetization of powdered samples was measured at 5 and 300 K with magnetic fields ranging from 70 to 70 kOe. The experimental data were corrected for diamagnetism of the constituent atoms, by using Pascal tables, and a sample holder.

Table 1 Crystal data and structure refinement parameters of $RbCu(HCO_2)_2Cl$

Crystal data	
Chemical formula	$C_2H_2ClCuO_4Rb$
M_r (g mol^{-1})	274.5
Crystal system; space group	Monoclinic; $P2_1/n$
Temperature (K)	300
a, b, and c (Å)	8.242 (2), 7.979 (2), and 9.723 (2)
β (°)	95.40 (3)
V (Å^3)	636.5 (3)
Z	4
Radiation type	Mo Kα
μ (mm^{-1})	11.38
Data collection	
Diffractometer	Xcalibur, AtlasS2, and Gemini ultra
T_{min}; T_{max}	0.575; 1
No. of measured, independent and observed [$I > 3\sigma(I)$] reflections	9955, 1645, and 1329
R_{int}	0.041
$(\sin\theta/\lambda)_{max}$ (Å^{-1})	0.691
Refinement	
$R[F^2 > 2\sigma(F^2)]$, $wR(F^2)$, and S	0.023, 0.058, and 1.30
No. of reflections	1645
No. of parameters	83
H-atom treatment	H-atom parameters constrained
$\Delta\rho_{max}$; $\Delta\rho_{min}$ (e Å^{-3})	0.46; −0.54

3. Results and discussion

3.1. Crystal structure

The green single crystals of $RbCu(HCO_2)_2Cl$ were prepared by a facile slow diffusion solution process at room temperature. Single-crystal X-ray diffraction (SCXRD) studies reveal that the compound crystallizes in a monoclinic system with space group $P2_1/n$, a = 8.242(2) Å, b = 7.979(2) Å, c = 9.723(2) Å, β = 95.40(3)° and V = 636.5(3) Å^3 at 300.1 K. **1** shows a well-known paddle-wheel structure typical of copper formates (Fig. 1A). The asymmetric unit contains one alkali metal (Rb^+) and a binuclear copper(II) paddle-wheel (PW), which contains two Cu^{2+} ions *syn–syn* connected *via* four oxygen atoms from four different formate groups, $Cu_2(HCOO^-)_4$. Each Cu(II) atom is also coordinated with a disordered chloride ion in the apical position, contributing to the framework's charge-neutrality. The result is a slightly distorted CuO_4Cl square-pyramidal environment around each Cu(II) with a Cu···Cu intramolecular distance of 2.7070(7) Å in the binuclear unit (Fig. 1B), as described for the isostructural $CsCu(HCOO)_2Cl$[29] and close to that of other compounds with similar structures.[12,21,22] In these square-pyramidal geometries, the copper ions Cu(II) lie above the basal plane towards the apical chloride ions. In addition, the planes of basal bonds around the copper ions are parallel to one another (Fig. 1C). This typical structure represents the simplest possible paddle-wheel geometry and is widely known as copper formate.[15,30,31]

The values of the bond distances (Å) and bond angles (°) are shown in Table 2. The $Cu–O_{formate}$ bond lengths range from 1.9624 (2) to 2.0075 (2) Å (Fig. 1B and Table 2). The apical bond distance in Cu–Cl is 2.3981 (12) Å. These bond length values agree with those in other binuclear Cu(II) compounds.[13,24,29,32] The bond angles $Cl_{(eq)}–Cu–O_{formate}$ range from 92.30 (7) to 101.42 (7)° (Table 2). The formate moieties have rather common bond angles, 126.9 (3)° for O2–C1–O3^{iii} and 127.5 (3)° for O1–C2–O4^{vi} (Table 2). The bond angle for the moiety Cl1–Cu2–Cu2 is 168.943 (6)°, showing a small deviation from linearity along the Cu–Cu axis.

In a unit cell, besides the two binuclear paddle-wheel (PW) copper(II) moieties, there are four Rb^+ cations located in the empty spaces within the three-dimensional framework formed

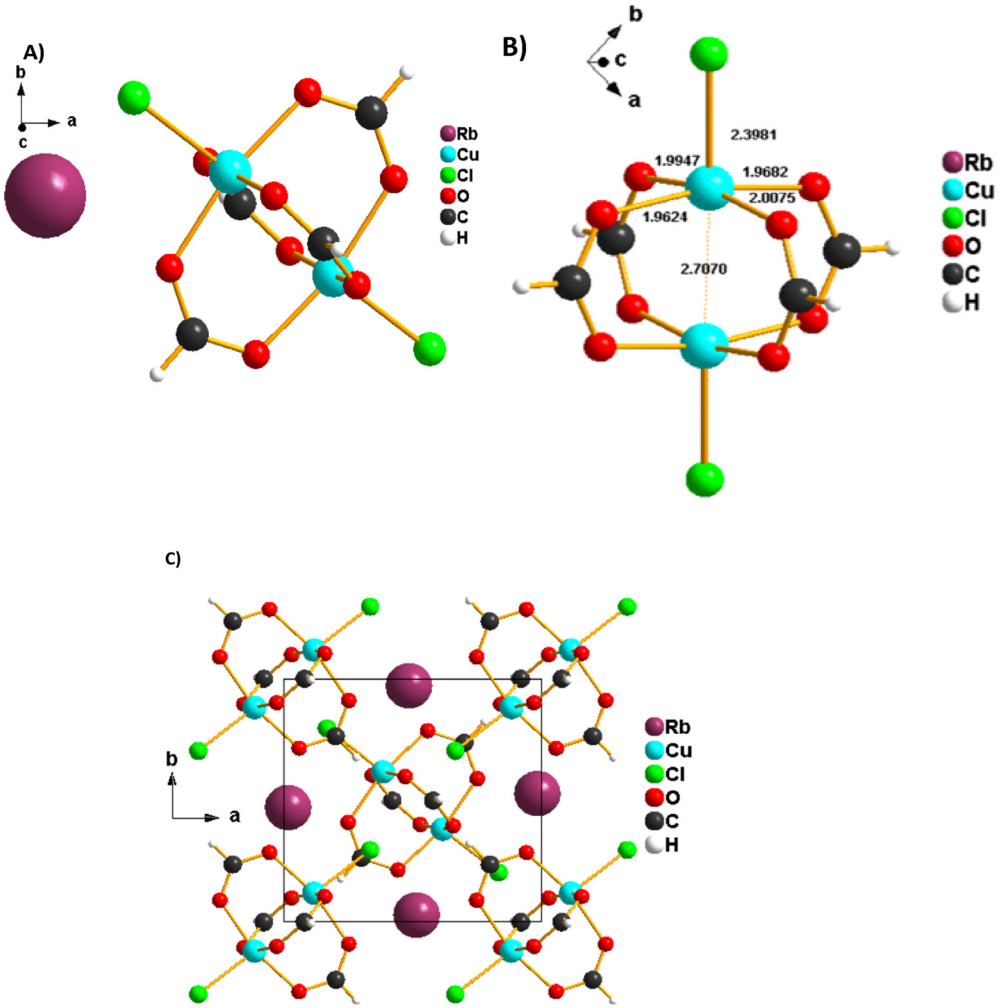

Fig. 1 (A) Molecular structure of $RbCu(HCO_2)_2Cl$. (B) Selected bond lengths (unit: Å) of Cu in the dinuclear (PW) copper(II) moieties. (C) Three-dimensional view of the crystal structure of **1** illustrates the local coordination of Cu in the dinuclear (PW) copper(II) moieties.

by the binuclear paddle-wheel (PW) copper(II) units (Fig. 2). The dinuclear PW units together with the Rb^+ cations form a herringbone arrangement when viewed down the *a*-axis. The Rb^+ cations, responsible for the charge balance of the Cu-based compound as counter ions, are bonded to four binuclear paddle-wheel $Cu_2(HCOO^-)_4$ dimers *via* formate oxygen and chloride anions through Rb–O and Rb–Cl electrostatic interactions. This results in an extended three-dimensional coordination framework. These coordination linkages connect adjacent PW units into zigzag infinite chains parallel to the *a*-axis, thereby reinforcing the overall structural stability of the network. The overall supramolecular arrangement, dominated by electrostatic interactions, is comparable to that of $CsCu(HCOO)_2Cl$.[29] In contrast, in the $[NH_3(CH_2)_nNH_3][Cu_2(HCOO)_4Cl_2]$ metal–organic compounds (n = 3 and 4), structural stability is primarily ensured by N–H···O and N–H···Cl^- H-bond interactions.[33]

Table 2 Geometric parameters (Å, °) for $RbCu(HCO_2)_2Cl$

Cu2–Cl1	2.3981 (12)	Cu2–O2	1.962 (2)
Cu2–O1^{i}	2.008 (2)	Cu2–O3	1.968 (2)
O1–C2	1.245 (4)	Cu2–O4	1.995 (2)
O2–C1	1.255 (4)	O3–C1^{iii}	1.255 (4)
C1–H1c1	0.96	O4–C2^{iv}	1.253 (4)
C2–H1c2	0.96	Cl1–Cu2–O2	101.42 (7)
Cl1–Cu2–O1^{i}	92.35 (7)	Cl1–Cu2–O3	92.30 (7)
Cl1–Cu2–O4	101.29 (7)	Cu2–O2–C1	119.3 (2)
O1^{i}–Cu2–O2	88.58 (9)	Cu2–O3–C1^{iii}	127.2 (2)
O1^{i}–Cu2–O3	91.45 (9)	Cu2–O4–C2^{iv}	119.4 (2)
O1^{i}–Cu2–O4	166.34 (9)	O2–C1–O3^{iii}	126.9 (3)
O2–Cu2–O3	166.26 (10)	O2–C1–H1c1	116.54
O2–Cu2–O4	88.07 (9)	O3^{iii}–C1–H1c1	116.54
O3–Cu2–O4	88.69 (9)	O1–C2–O4^{vi}	127.5 (3)
O1–C2–H1c2	116.23	O4^{vi}–C2–H1c2	116.23
Cu2^{i}–O1–C2	126.3 (2)		

Symmetry codes: (i) $-x, -y+1, -z+1$; (ii) $x-1/2, -y+3/2, z-1/2$; (iii) $-x+1, -y+1, -z+1$; (iv) $x+1, y, z$; (v) $x+1/2, -y+3/2, z+1/2$; (vi) $x-1, y, z$.

3.2. Vibrational properties

Fig. 3 exhibits the room-temperature IR spectrum of $RbCu(HCO_2)_2Cl$, while Table S3 exhibits the values of the IR absorption band frequencies and their assignment. The IR spectrum exhibits all the strongest characteristic formate vibration bands. It is well known that the HCO_2^- ions have six

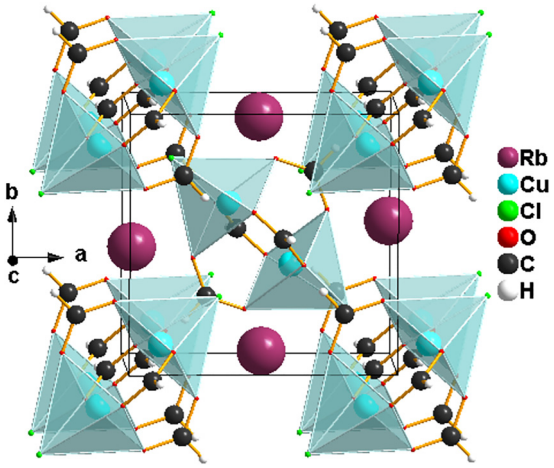

Fig. 2 Polyhedral presentation of the coordination environments of the Cu in $RbCu(HCO_2)_2Cl$. The 3D-framework cavities, formed by the dinuclear paddle-wheel (PW) copper(II) units, are occupied by Rb^+ cations.

internal modes: the ν_1 C–H stretching mode, the ν_2 symmetric C–O stretching mode, the ν_4 antisymmetric C–O stretching mode, the ν_3 symmetric O–C–O bending (scissor) mode, the ν_5 C–H in-plane bending mode and the ν_6 C–H out-of-plane bending mode.[34,35] These modes were observed in narrow wavenumber ranges for different metal formate frameworks.[36,37] In the high wavenumber region, besides the $\nu_1(HCO_2)$ mode, others expected bands attributed to some combinations and overtones of other $\nu(HCO_2)$ modes can be observed. From Fig. 3, the vibrations bands at 2895 and 2845 cm^{-1} are assigned to the stretching mode $\nu_1(HCO_2)$, while the IR spectrum shows two very weak vibration bands at 2976 and 2945 cm^{-1} that are related to the combination of the $\nu_4(HCO_2)$ and $\nu_5(HCO_2)$ modes, and the overtones $2\nu_5$ and $2\nu_2$, respectively. The strong bands observed at 1614 and 1552 cm^{-1} in the medium wavenumber region could belong to the ν_4(HCOO) asymmetric C–O stretching modes of the CO_2^- moiety. The C–H in-plane bending mode $\nu_5(HCO_2)$ is observed as medium IR bands in the region 1413–1376 cm^{-1}. Additionally, the intense vibration band located at 1337 cm^{-1} is assignable to the symmetric C–O stretching mode $\nu_2(HCO_2)$. In the spectrum, a significant shift in the ν(C–O) and ν(C=O) stretching can be observed in reference to the spectra of free formate ions (HCO_2^-), confirming the coordination of copper(II) ions with the formate groups. The modes observed in the lower wavenumber region at 1045 and 769 cm^{-1} are assigned to the out-of-plane C–H bending mode $\nu_6(HCO_2)$ and the symmetric O–C–O bending mode $\nu_3(HCO_2)$, respectively. Finally, the strong vibration band observed at 403 cm^{-1} is due to the Cu–O bond. These results agree well with those reported for other Cu-based formate frameworks.[38–40]

3.3. Thermal properties

The thermal stability of $RbCu(HCO_2)_2Cl$ was investigated using combined thermogravimetric analysis (TGA) and differential thermal analysis (DTA) results from experiments on a crystalline powder sample in an air atmosphere at a heating rate of 10 K min^{-1}, from 315 to 780 K (Fig. 4). The TGA results reveal that **1** is thermally stable up to 350 K, and above this temperature, it begins to decompose in one main mass loss step, as observed in the TGA curve (red curve in Fig. 4). The experimental percent weight loss is approximately 31.67%, which is close to the expected (calculated) loss of two formate ligands per formula unit (theoretical value: 32.78%). This decomposition is found to be exothermic, as indicated by the DTA, which displays an exothermic peak at 426 K (green curve in Fig. 4). This result is similar to the one reported for $CsCu(HCO_2)_2Cl$, in which the degradation occurs in one main weightless step at approximately 425 K.[29] During the whole decomposition process of compound **1**, the resulting formed residue corresponds to binary (RbCl) and metallic Cu species. These results align well with the observed thermal behavior of other Cu-containing formate-based alkali metals, where decomposition occurs over very small temperature intervals and at low onset temperatures.[40,41] Additionally, a small mass degradation is observed in the TGA curve at higher temperatures, which could be attributed to internal redox reactions where copper is reduced. Subsequently, the residue remains nearly stable up to 500 K.

3.4. Magnetic properties

Variable temperature magnetic susceptibility measurements were performed on powdered samples of $RbCu(HCO_2)_2Cl$ in

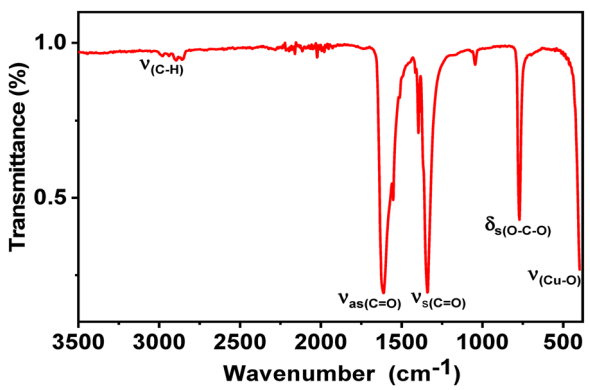

Fig. 3 Room-temperature IR spectrum of $RbCu(HCO_2)_2Cl$.

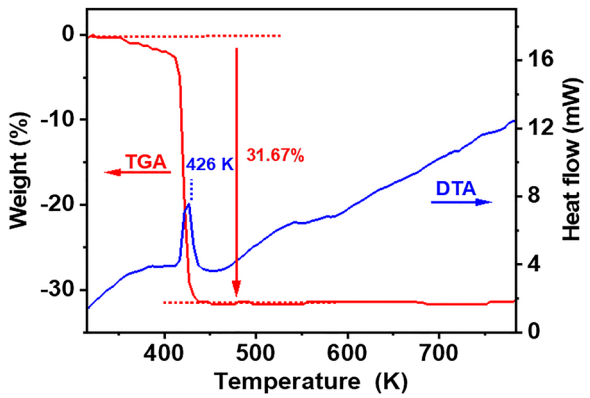

Fig. 4 Combined TGA–DTA curves of $RbCu(HCO_2)_2Cl$.

the temperature range 5–300 K. Plots of the thermal evolution of the magnetic molar susceptibility (χ_m) and the $\chi_m T$ product ($\chi_m T = \mu_{eff}^2/8$) are shown in Fig. 5. At room temperature, $\chi_m T$ is equal to 0.11 cm^3 K mol^{-1} ($\mu_{eff} = 0.94\mu_B$), a value significantly lower than the theoretical spin-only value for an $S = 1/2$ system (0.375 cm^3 K mol^{-1}). Upon cooling, $\chi_m T$ continuously decreases, and it practically vanishes at low temperatures ($\chi_m T = 0.002$ cm^3 K mol^{-1} at 5 K). The susceptibility decreases from 300 to 80 K and rapidly increases as the temperature is lowered further to 5 K, probably due to the small amount of the paramagnetic Cu(II) compound detected in the EPR study. This behavior is consistent with a strong antiferromagnetic coupling between the two Cu^{2+} ions linked by four formate groups that form the Cu_2 paddle-wheel units that give rise to the anionic network in this compound. Therefore, we tried to fit the susceptibility data using the Bleaney–Bowers equation for a Cu(II) dimer[42] (eqn (1)) combined with an additional term accounting for a paramagnetic contribution, assumed to come from a species with the same molecular weight per Cu(II) ion and g-value as the main compound to avoid overparameterization:[43]

$$\chi_m = (1-\delta)\frac{Ng^2\beta^2}{kT}\frac{1}{3+\exp(-J/kT)} + \delta\frac{Ng^2\beta^2}{4kT} \quad (1)$$

where J is the singlet–triplet energy gap, defined by the spin Hamiltonian $H = -JS_1 \cdot S_2$ ($S_1 = S_2 = 1/2$), g is the Lande g factor and ρ is the percent of noncoupled impurity; N, β, and k are Avogadro's number, the Bohr magneton, and Boltzmann's constant, respectively. The best-fit parameters obtained by minimizing the reliability R factor, $R = \sum\left[(\chi_m T)_{exp} - (\chi_m T)_{cal}\right]^2 \Big/ \sum\left[(\chi_m T)_{exp}\right]^2$, are $J = -531$ cm^{-1}, $g = 2.125$ and $\delta = 0.0047$, with $R = 2.8 \times 10^{-5}$. As shown in Fig. 5, the fitting curves reproduce the experimental magnetic data very well over the whole temperature range investigated. The obtained singlet–triplet energy gap is close to the average value ($J = -550$ cm^{-1}) determined for copper carboxylate complexes with the same core, although it is somewhat larger than that calculated ($J = -425$ cm^{-1}) for a model compound [$Cu_2(\mu$-$HCOO)_4(H_2O)_2$] with an intradimeric Cu–Cu distance of 2.707 Å.[44]

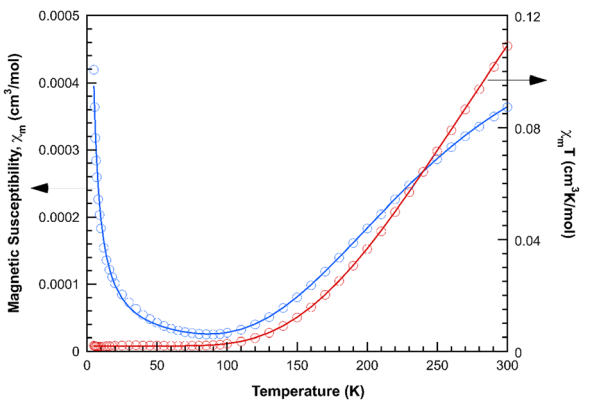

Fig. 5 Magnetic behavior of compound $RbCu(HCO_2)_2Cl$. The solid lines represent the best least-squares fit to experimental data (see text for details of the fit).

This is due to the presence of chloride ions as axial ligands and to slight differences in the geometry of the carboxylate bridges arising from the Rb–Cl and Rb–O bonds, which stabilize the three-dimensional framework. Despite the short Cu–Cu distance, super exchange is the dominant coupling mechanism in Cu dimers with the *syn–syn* coordination mode of the formate groups because the unpaired electron on each copper(II) ion occupies parallel $d_{x^2-y^2}$ orbitals oriented towards the oxygen atoms of the bridging ligands. Therefore, the coupling constant can be strongly affected by small structural changes in this type of compound.

Notably, this compound does not exhibit the complex magnetic behavior observed for the isostructural $CsCu(HCOO)_2Cl$ material.[29] The susceptibility curves recorded on zero-field cooled (ZFC) and field-cooled (FC) samples show no signs of irreversibility above 5 K. Furthermore, there is no indication of a magnetic transition, such as those observed at 8 and 32 K in the aforementioned compound. At room temperature, the field-dependent magnetization displays a straight line as expected for a classic paramagnetic compound (not shown). A small ferromagnetic anomaly can be detected in the magnetization measurements at 5 K, but it is practically negligible (see Fig. S3). In fact, the magnetization curve at 5 K can be reasonably well described by the Brillouin function for a system with $S = 1/2$ normalized to account for the percentage of paramagnetic impurity deduced from the susceptibility fit.[45]

Considering the strong antiferromagnetic coupling between the two metallic ions within paddle-wheel dinuclear copper carboxylates, ferromagnetic orderings are not expected in systems with these building blocks. In fact, the sudden increase in the magnetic susceptibility frequently observed at low temperatures is usually ascribed to paramagnetic impurities resulting from the synthetic procedure.[43] However, more complex magnetic properties have been observed in some coordination polymers containing that type of dimeric entity, including spontaneous magnetization.[46–48] Such behavior has been interpreted in terms of a weak ferromagnetic coupling between the dimers or canted antiferromagnetic ordering due to the competition of different intra and interdimeric interactions. But these interpretations are questioned by several authors because of the essentially molecular character of the $Cu_2(COO)_4$ units in most of these compounds.[49] Due to strong antiferromagnetic interactions, dimers do not possess a net spin moment at low temperatures that could give rise to weak ferromagnetism or canted ordering. In fact, theoretical calculations by Shen *et al.*[50] show that the energy barrier necessary to create a net magnetic moment in such dimers would be impossible to overcome at temperatures close to 5 K. These authors have shown that the ferromagnetism observed in certain MOFs with paddle-wheel units linked by conjugated aromatic ligands has its origin in the existence of copper vacancies that allow the existence of localized magnetic moments. The ferromagnetic ordering is achieved *via* π-electrons of the aromatic linkers that connect the copper-defective dimers. Moreover, it is well known that, in other Cu oxides, Cu or oxygen vacancies produce local moments that enhance ferromagnetism.[51,52] According to this model, the presence of a very small number of copper vacancies

in the title compound could be the reason why it does not show the weak ferromagnetism described for the isostructural $CsCu(HCOO)_2Cl$. It should be noted that vacancies are an inevitable feature of structurally complex systems such as these, but their concentration is strongly influenced by the preparation procedure.

3.5. Electron paramagnetic resonance behavior

The Q-band (300 K) and X-band (300, 175 and 5 K) powder EPR spectra of $RbCu(HCO_2)_2Cl$ are displayed in Fig. 6A and B, respectively. A set of five broad anisotropic resonances is observed in the Q-band, centered at approximately 480, 650, 925, 1100 and 1380 mT. The X-band displays two intense signals at magnetic fields of approximately 85 and 500 mT, two weaker signals at around 30 and 590 mT, and a weak, complex band at approximately 315 mT. When the temperature is lowered to 5 K, only the latter can be detected. As is frequently observed for dinuclear copper complexes with carboxylate bridges, the recorded spectra exhibit the expected features of a triplet state ($S = 1$) with significant zero-field splitting (ZFS). Therefore, the following spin Hamiltonian (eqn (2)), which includes Zeeman electronic and ZFS terms,[53] has been used to analyze them:

$$\hat{H} = \beta B \boldsymbol{g} \hat{S} + \hat{S} \boldsymbol{D} \hat{S} = \beta B \boldsymbol{g} \hat{S} + D\left(S_z^2 - \frac{2}{3}\right) + E\left(S_x^2 - S_y^2\right) \quad (2)$$

where D and E are the axial and rhombic zero-field splitting parameters, respectively. As the Zeeman contribution in the X-band experiment is of the same order of magnitude as the ZFS in this type of dimeric entities,[54] we used the Q-band spectra to determine the eigen values of the g and D tensors. Adjusting the observed signals by the trial and error method, the following values were obtained: $g_{\parallel} = 2.375$; $g_{\perp} = 2.064$; $|D| = 0.414$ cm^{-1}; $|E| < 0.01$ cm^{-1}. These parameters were used to simulate the Q-band EPR spectrum, producing the dashed line in Fig. 6A, and to identify and label the observed peaks using the standard notation for copper dimers with approximate axial symmetry.[55] We have also identified the so-called "half-field signal", which corresponds to the transition between the $M_s = -1$ and $M_s = +1$ states ($\Delta M_s = \pm 2$). This signal is formally forbidden by the EPR spectroscopy selection rule ($\Delta M_s = \pm 1$) and not generated by our simulation program. The calculated g-values are typical of Cu(II) ions in square-pyramidal environments with the unpaired electron on the $d_{x^2-y^2}$ orbital. The absolute value of D is at the upper end of the range usually observed for copper carboxylate dimers, as is also the case for other formate compounds.[56]

The sign of the D parameter cannot be determined using low-frequency EPR or magnetic susceptibility measurements, particularly in strongly antiferromagnetic systems, which become practically EPR-silent at low temperatures. However, we assume that D is negative for this compound since Ozarowski has shown by high-frequency single-crystal EPR studies that this parameter appears to be negative for all binuclear copper carboxylates exhibiting paddle-wheel structures.[56] The zero-field splitting of the $S = 1$ state in these compounds arises from the combined effect of spin dipolar interactions and anisotropic exchange couplings between one electron in the ground state and another one in an excited state. Therefore, the calculated D value can be evaluated as $D = D_{dip} + D_{ex}$. Considering that in this type of dimers the Cu···Cu direction practically coincides with the z-axis of the g-tensor, the dipolar contribution can be estimated from the distance between metals (r) using eqn (3).[57]

$$D_{dip} = -\frac{2g_z^2 + \left(g_x^2 + g_y^2\right)/2}{2r^3}\beta^2 \quad (3)$$

Using the values of g deduced from the EPR fit and the distance $r_{(Cu\cdots Cu)} = 2.707$ Å from the structural resolution, a value of $D_{dip} = -0.149$ cm^{-1} is obtained from the above expression. Therefore, the exchange contribution to the ZFS is $D_{ex} = -0.265$ cm^{-1}. This value can be used to determine the

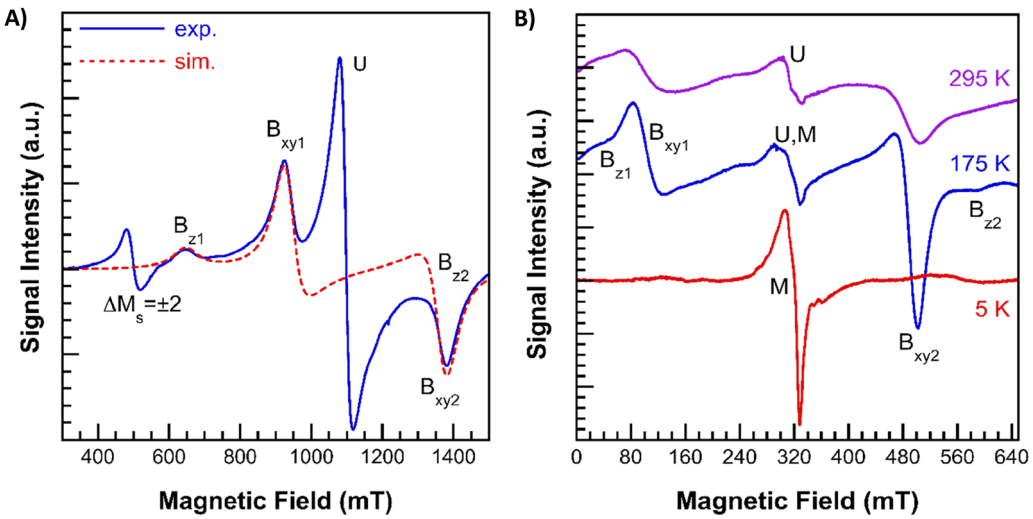

Fig. 6 EPR spectra of $RbCu(HCO_2)_2Cl$ powder at (A) 33.9 GHz and 295 K and (B) 9.4 GHz at 295, 175 and 5 K. Dotted-red line in A is a simulation with the parameters indicated in the text.

triplet–singlet separation in dimeric excited states where one cupric ion is in its electronic ground state ($d_{x^2-y^2}$) while another one is in an excited state (d_{xy}, d_{xz}, and d_{yz}).[58] It is noteworthy that the relationship between D_{ex} and the exchange integral (J) is still unknown, although a correlation between both values has been observed.[59]

The intense line appearing at around 1100 mT in the Q-band spectrum and labeled "U" does not correspond to any of the expected transitions within a triplet $S = 1$ state. This signal is too intense to be entirely attributed to the presence of a paramagnetic impurity. Furthermore, its relative intensity decreases with temperature, contrary to what would be expected for such a contribution. Additionally, spectra obtained at various microwave powers suggest that all signals exhibit comparable saturation properties, indicating that they originate from the same magnetic system. Similar resonances have been observed in polymeric structures built on copper dinuclear paddle-wheel units and have been attributed to extended exchange signals originating from the collapse of the fine structure due to interdimeric interactions.[60–63] Exchange magnetic couplings between the spins of neighbouring units can average out the zero-field splitting if they are strong enough. Otherwise, the lines could only collapse for certain crystal orientations. Therefore, spectra recorded in powder samples could show both exchange and molecular resonances. Additionally, interdimeric interactions compete with the strong intradimeric antiferromagnetic couplings characteristic of these compounds. As the population of the excited $S = 1$ state rises with increasing temperature, the distance between the dimers with net spin moment decreases. This leads to a more efficient exchange process between the dimers, which in turn results in an increase in the intensity of the exchange signal "U", at the expense of the ZFS lines. Considering that the exchange signal is not observable below 100 K in the $RbCu(HCOO)_2Cl$ compound, it can be concluded that the increase in magnetic susceptibility observed at low temperatures is not caused by interdimeric interactions.

Finally, it should be noted that, as the temperature decreases, the relaxation time increases and all the peaks of the spectra become narrower, except for the one corresponding to the extended exchange signal. This improves the resolution of the spectra, even though the intensity of the signals decreases (Fig. S4). Below 75 K, the signals corresponding to the triplet state are no longer detectable, confirming the presence of strong intradimeric antiferromagnetic interactions. At 5 K, only the characteristic signal of magnetically isolated Cu(II) ions (labeled "M") is observed (Fig. S5). The hyperfine structure resulting from the interaction of the $S = 1/2$ electron spin with the nuclear magnetic moments of the ^{63}Cu and ^{65}Cu isotopes ($I = 3/2$) is partially resolved on the low-field region of the signal. The spin Hamiltonian parameters obtained from the fitting of the powder spectra are: $g_1 = 2.360$, $g_2 = 2.111$, $g_3 = 2.044$, $A_1 = 0.0140$ cm^{-1}, $A_2 = 0.0041$ cm^{-1}, and $A_3 < 0.0010$ cm^{-1}. The calculated g-values indicate that these ions are in the same ground state ($d_{x^2-y^2}$) as those forming the dimer, but the environment is notably different in the equatorial plane. EPR signals from mononuclear Cu^{2+} ions in compounds with paddle-wheel units are usually observed and attributed to extra-framework impurities. Nevertheless, it cannot be ruled out that the spectrum is due to the existence of copper vacancies that convert some of the dimers into monomers. In any case, the observed increase in magnetic susceptibility below 70 K (Fig. 5) is due to these isolated Cu(II) ions.

3.6. Evaluation of antibacterial activity

The antibacterial activity of $RbCu(HCO_2)_2Cl$ was evaluated *in vitro* against two Gram-positive bacteria, *S. aureus* CECT 86 and *L. monocytogenes* CECT 4031, and two Gram-negative bacteria, *E. coli* CECT 99 and *K. pneumoniae* CECT 143^T, using both the disc diffusion and the agar well diffusion methods. For both, 20 μL of a sterile 15 mg mL^{-1} solution of **1** were used. Table 3 shows the values of the inhibition halo diameter from both methods (see Fig. S6) and those from the commercial discs of antibiotics used as the positive control for each of the bacteria. It is worth noting that the diameters obtained for Gram-positive bacteria were higher than those for Gram-negative in both methods.

Comparison of values from the disc diffusion method with those from the commercial discs of antibiotics displayed the lower antibacterial activity of **1** against all the bacteria, except for *L. monocytogenes* CECT 4031, for which the diameters of the halos obtained were similar. The diameters of halos from the

Table 3 Mean values ($n = 2$) of the diameters of the inhibition halos (mm) obtained in the phenotypic assays using $RbCu(HCO_2)_2Cl$ and commercial antibiotic discs

	Inhibition halo diameter (mm)			
	Gram-positive bacteria		Gram-negative bacteria	
	S. aureus CECT 86	*L. monocytogenes* CECT 4031	*E. coli* CECT 99	*K. pneumoniae* CECT 143^T
Disc diffusion method	12	15	9	8
Agar well diffusion method	25	27	15	15
Norfloxacin (5 μg)	19			
Vancomycin (30 μg)	14.5			
Gentamicin (10 μg)		15		17.5
Ampicillin- sulfactam (10/10 μg)		16		
Trimethoprim-sulfamethoxazole (25 μg)			16	
Nitrofurantoin (300 μg)			18	
Ciprofloxacin (5 μg)				24.5

agar well diffusion method were, for all the bacteria, greater than those from the disc diffusion method, even though the quantity of **1** used was the same. It could be due to a better diffusion of the compound in the agar from the wells. Fig. 7 shows the results from the quantitative assay to determine the MIC of **1**. It is clear that **1** was able to inhibit the growth of both Gram-positive and Gram-negative bacteria, though the decrease of growth varied with the species and with the concentration. For all the bacteria, except for *S. aureus* CECT 86, the growth was inversely proportional to the concentration of **1**, as reported in other studies.[64] In the case of *S. aureus* CECT 86, the maximum decrease was obtained at a concentration of 800 μg mL^{-1}. Using larger concentrations did not produce a significant increase in growth inhibition, with values remaining stable around 20%.

The concentrations that were assayed appear to be significantly above the MIC, as the percentages of growth decrease were less than fifty percent for three of the four bacteria tested. Concentrations above 1000 μg mL^{-1} were more effective against *L. monocytogenes* CECT 4031, achieving a growth reduction of 54.02% at the highest concentration tested, followed by *E. coli* CECT 99 and *K. pneumoniae* CECT 143^{T}. It might be advisable for future studies to use higher concentrations along with toxicity assessments of **1**.

In reference to the measurement of the DO_{600} during the incubation of the strains at different concentrations of **1**, it is worth noting that when *E. coli* CECT 99 was grown in the presence of 2500 μg mL^{-1} of **1**, the DO_{600} remained constant during the 24 h of incubation and the counts of viable cells at the end of incubation showed that the cells from the inoculum had remained alive without showing growth. This observation suggests that **1** at this concentration has a bacteriostatic effect. A similar result was observed for *L. monocytogenes* CECT 4031 at concentrations of 2000 and 2500 μg mL^{-1}.

With respect to the antibacterial activity of the copper compounds, some authors reported that it depends on the geometry of the complexes and the nature of the ligands, because both factors influence the lipophilic character of the compounds, affecting their permeability through the cytoplasmic membrane.[65,66] The mechanism of action described for these compounds are diverse although in many respects still unknown.[67] For example, it has been suggested that the release of copper ions causes the inactivation of enzymes,[68] and more recently that the metallic chelates of Cu^{2+} act disturbing the microbial metabolism and producing their destruction.[17] Other possible mechanisms include damage to DNA by reactive oxygen species (ROS) produced through Fenton-type reactions, as well as a decrease in cell membrane integrity.[10,17] Differences observed in the activity against Gram-positive and Gram-negative bacteria may stem from variations in the structure and chemical composition of their cell walls, as noted for other metallic compounds.[69]

The antibacterial activity of metal-based complexes can be rationalized using chelation theory and Tweedie's polarization model.[16,70–74] Typically, the chelation modifies metal ion properties, enhancing membrane penetration and polarization-induced reactive oxygen species (ROS) generation, which together account for the superior antibacterial activity of metal complexes.[16] For the present compound, the antibacterial activity arises from synergistic structural and electronic effects. We suggest that chelation of Cu(II) by bridging formate ligands delocalizes the positive charge over oxygen atoms, reducing the metal center's polarity and enhancing its lipophilicity relative to the hydrated Cu^{2+} ion. This favours interaction with bacterial surfaces and membrane penetration. According to Tweedie's model, the Cu–formate environment also promotes polarization of negatively charged bacterial membranes, facilitating copper uptake.[70] Additionally, the distorted Cu^{2+} sites may undergo Cu^{2+}/Cu^{+} redox cycling, generating ROS that damage key biomolecules.[16]

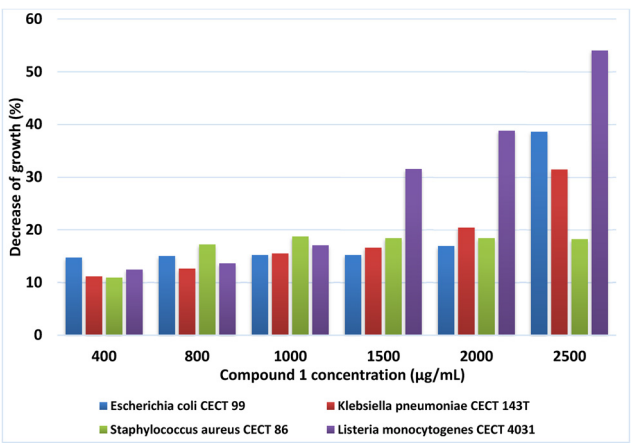

Fig. 7 *In vitro* antimicrobial activity of $RbCu(HCO_2)_2Cl$ at different concentrations against two Gram-negative and two Gram-positive bacteria.

4. Conclusion

To conclude, a new copper(II)-based MOF paddle-wheel-like compound, $RbCu(HCO_2)_2Cl$, was successfully synthesized and characterized using spectroscopic, thermal, and magnetic techniques. Single-crystal X-ray diffraction revealed that **1** crystallizes in a monoclinic system with a 3D framework built from dinuclear Cu(II) paddle-wheel units, where each Cu(II) center adopts a square-pyramidal geometry with a Cu···Cu distance of 2.7070(7) Å. The Rb^{+} cations serve as counter-ions, ensuring charge balance within the framework. The thermal stability of **1** was studied. Upon further heating of **1**, its resulting residue corresponds to binary (RbCl) and metallic Cu species. Magnetic studies revealed strong intradimer antiferromagnetic exchange coupling ($J = -531$ cm^{-1}) between the Cu^{2+} centers, corroborated by EPR spectra showing characteristic triplet-state ($S = 1$) features with zero-field splitting. The *in vitro* antibacterial tests against *S. aureus*, *L. monocytogenes*, *E. coli*, and *K. pneumoniae* demonstrated both bacteriostatic and bactericidal activity, suggesting its potential as a promising antimicrobial agent. Overall, these findings highlight the multifunctional nature of this Cu(II)-based paddle-wheel MOF, encouraging further investigation into its magnetic behavior and the development of related bioactive coordination materials for potential biological applications.

Author contributions

Asmae Ben Abdelhadi: writing – original draft, methodology, investigation, and formal analysis. Safaa Hidaoui: investigation. Rachid Ouarsal: writing – review & editing, validation, methodology, and formal analysis. Morgane Poupon: software and formal analysis. Michal Dusek: software and formal analysis. María de los Llanos Palop Herreros: investigation, writing – review & editing, validation, methodology, and formal analysis. Marco Antonio López de la Torre: methodology, investigation, and formal analysis. Luis Lezama: writing original draft, validation, methodology, investigation, and formal analysis. Brahim El Bali: conceptualization, validation, formal analysis, and writing – review & editing. Mohammed Lachkar: supervision, project administration, resources, methodology, investigation, and formal analysis, validation and writing – review & editing. Abderrazzak Douhal: supervision, conceptualization, project administration, resources, methodology, investigation, and formal analysis, validation and writing – review & editing. All authors read and approved the manuscript.

Conflicts of interest

There are no conflicts of interest to declare.

Data availability

The data supporting this article have been included as part of the supplementary information (SI). Supplementary information is available. See DOI: https://doi.org/10.1039/d5ma01055a.

CCDC 2468965 (**1**) contains the supplementary crystallographic data for this paper.[75]

Acknowledgements

This work was supported by the following grants: PID2020-116519RB-I00 funded by MICIU/AEI/10.13039/501100011033 and the European Union (EU) and SBPLY/23/180225/000196 funded by the JCCM and the EU through Fondo Europeo de Desarrollo Regional (FEDER). A. B. A. is grateful for the grant from the Spanish Service for the Internationalization of Education (SEPIE), through the EU Erasmus+ Key Action program (2020-1-ES01-KA107-079868). The authors A. B. A., S. H., R. O., B. E. B. and M. L. would like to acknowledge the technical assistance from the Interface Regional University Center (University Sidi Mohammed Ben Abdellah, Fez, Morocco). Crystallographic analysis was supported by the project 20-LM2023051 of the Czech Nanolab Infrastructures, supported by MEYS CR.

References

1 J. Annamalai, P. Murugan, D. Ganapathy, D. Nallaswamy, R. Atchudan, S. Arya, A. Khosla, S. Barathi and A. K. Sundramoorthy, *Chemosphere*, 2022, **298**, 134184.
2 Q. Zhang, S. Yan, X. Yan and Y. Lv, *Sci. Total Environ.*, 2023, **902**, 165944.
3 D. Li, A. Yadav, H. Zhou, K. Roy, P. Thanasekaran and C. Lee, *Global Challenges*, 2024, **8**, 2300244.
4 M. Mendt, M. Maliuta, S. Ehrling, F. Schwotzer, I. Senkovska, S. Kaskel and A. Pöppl, *J. Phys. Chem. C*, 2022, **126**, 625–633.
5 N. Ahmad, H. A. Younus, A. H. Chughtai, K. Van Hecke, Z. A. Khattak, Z. Gaoke, M. Danish and F. Verpoort, *Catal. Sci. Technol.*, 2018, **8**, 4010–4017.
6 T. Zanette, Y. M. Variani, B. P. Nicola, S. Gutiérrez-Tarriño, C. Cerezo-Navarrete, G. Agostini, P. Oña-Burgos, C. W. Lopes and K. Bernardo-Gusmão, *Catal. Today*, 2025, **444**, 114988.
7 T.-R. Lin, C.-H. Lee, Y.-C. Lan, S. Mendiratta, L.-L. Lai, J.-Y. Wu, K.-M. Chi and K.-L. Lu, *Polymers*, 2018, **10**, 1398.
8 Z. Zhang, H. Yu, X. Shen, L. Sun, S. Yue and H. Tang, *Materials*, 2021, **14**, 3125.
9 M.-H. Yan, J. Wang, X.-Y. Su, H. Sakiyama, N. Qi, M. Afzal, A. Alarifi, D. Srivastava and A. Kumar, *New J. Chem.*, 2023, **47**, 11134–11142.
10 A. L. Pereira, M. A. Vasconcelos, A. L. Andrade, I. M. Martins, A. K. Holanda, A. C. Gondim, D. P. Penha, K. L. Bruno, F. O. Silva and E. H. Teixeira, *Curr. Microbiol.*, 2023, **80**, 133.
11 Viola, N. Muhammad, A. Noor, M. Sirajuddin, M. Kubicki, S. Rahim, A. Samad, S. Shujah, A. Wadood and S. Ali, *Pharmaceuticals*, 2023, **16**, 1462.
12 F. Li, K. Liu, S. Fan, T. Qin, S. Xiong and J. Wang, *Z. Anorg. Allg. Chem.*, 2018, **644**, 560–563.
13 V. Paredes-García, R. C. Santana, R. Madrid, A. Vega, E. Spodine and D. Venegas-Yazigi, *Inorg. Chem.*, 2013, **52**, 8369–8377.
14 K. Ngece, V. Khwaza, A. M. Paca and B. A. Aderibigbe, *Antibiotics*, 2025, **14**, 516.
15 M. Premkumar, D. Kaleeswaran, G. Kaviyarasan, D. Prasanth and G. Venkatachalam, *ChemistrySelect*, 2019, **4**, 7507–7511.
16 M. S. Alhussaini, A. A. I. Alyahya and A. A. Al-Ghanayem, *Dyes Pigm.*, 2025, **243**, 113040.
17 B. Sharma, S. Shukla, R. Rattan, M. Fatima, M. Goel, M. Bhat, S. Dutta, R. K. Ranjan and M. Sharma, *Int. J. Biomater.*, 2022, **2022**, 6819080.
18 V. J. Tamilpriyai, P. Nagarasu, K. S. Dharshini, P. Dhanaraj, A. Veerappan, D. Moon, S. P. Anthony and V. Madhu, *J. Mol. Struct.*, 2023, **1294**, 136414.
19 D. Majumdar, S. Roy, J. Elizabeth Philip, B. Tüzün and S. Hazra, *Inorg. Chem. Commun.*, 2024, **160**, 111933.
20 S. Notz, K. Müller, R. Thomas, T. Rüffer and H. Lang, *Inorg. Chem. Commun.*, 2024, **167**, 112765.
21 J. Soldevila-Sanmartín, J. A. Ayllón, T. Calvet, M. Font-Bardia, C. Domingo and J. Pons, *Inorg. Chem. Commun.*, 2016, **71**, 90–93.
22 J. Zhou, L. Du, Z. Li, Y. Qiao, J. Liu, M. Zhu, P. Chen and Q. Zhao, *J. Coord. Chem.*, 2013, **66**, 2166–2177.
23 H. Phetmung and A. Nucharoen, *Polyhedron*, 2019, **173**, 114121.
24 E. Y. Bivián-Castro, M. Flores-Alamo, R. Escudero, V. Gómez-Vidal, J. J. N. Segoviano-Garfias, J. Castañeda-Contreras and Q. E. Saavedra-Arroyo, *Materials*, 2023, **16**, 4866.
25 S. M. Bovill and P. J. Saines, *CrystEngComm*, 2015, **17**, 8319–8326.
26 L. Palatinus and G. Chapuis, *J. Appl. Crystallogr.*, 2007, **40**, 786–790.

27 V. Petříček, L. Palatinus, J. Plášil and M. Dušek, *Z. Kristallogr. – Cryst. Mater.*, 2023, **238**, 271–282.
28 K. Brandenburg and H. Putz, Crystal Impact GbR, Bonn, Germany, 2006.
29 J. Zhou, S. Jin, R. Sun, C. Chai, M. Hao, X. Zhong and X. Chen, *Phys. Rev. Mater.*, 2021, **5**, 074405.
30 K. Karthik and A. M. Qadir, *J. Struct. Chem.*, 2019, **60**, 1126–1132.
31 A Qadir, *Orient. J. Chem.*, 2017, **33**, 968–970.
32 B. Saha, M. Bhattacharjee, S. R. Boruah, R. N. Dutta Purkayastha, R. M. Gomila, S. Chowdhury, A. Mandal and A. Frontera, *J. Mol. Struct.*, 2023, **1272**, 134104.
33 M. Trzebiatowska-Gusowska and A. Gagor, *J. Coord. Chem.*, 2017, **70**, 1–22.
34 C. W. A. Paschoal, M. R. Moura, A. P. Ayala, J. M. Sasaki, P. T. C. Freire, F. E. A. Melo, J. Mendes Filho, I. Guedes, A. G. Leyva, G. Polla, D. Vega and P. K. Perazzo, *J. Solid State Chem.*, 2000, **154**, 338–343.
35 M. A. Moreno, O. Gálvez, B. Maté, V. J. Herrero and R. Escribano, *J. Phys. Chem. A*, 2011, **115**, 70–75.
36 A. Ciupa and M. Ptak, *Vib. Spectrosc.*, 2016, **86**, 67–74.
37 M. Mączka, A. Ciupa, A. Gągor, A. Sieradzki, A. Pikul and M. Ptak, *J. Mater. Chem. C*, 2016, **4**, 1186–1193.
38 A. B. Abdelhadi, R. Ouarsal, M. Poupon, M. Dusek, J. P. A. González, L. Lezama, B. El Bali, M. Lachkar and A. Douhal, *Mater. Adv.*, 2024, **5**, 6154–6161.
39 A. P. Ayala, J. M. Henriques Neto, C. W. A. Paschoal, I. Guedes, J. M. Sasaki, P. T. C. Freire, F. E. A. Melo, J. Mendes Filho, A. G. Leyva, G. Polla, D. Vega and P. K. Perazzo, *J. Raman Spectrosc.*, 2000, **31**, 491–495.
40 Y. Abusa, J. Greenfield, G. Viswanathan, S. Goswami, E. Ross, P. Yox, R. Oppong, I. Ojo, J. Liu, A. Ozarowski and K. Kovnir, *Chem. Sci.*, 2025, **16**, 11027–11038.
41 E. Eikeland, N. Lock, M. Filsø, M. Stingaciu, Y. Shen, J. Overgaard and B. B. Iversen, *Inorg. Chem.*, 2014, **53**, 10178–10188.
42 B. Bleaney and K. Bowers, *Proc. R. Soc. London, Ser. A*, 1952, **214**, 451–465.
43 O. Kahn, *Molecular magnetism*, VCH Publishers Inc., New York, 1993, pp. 167–174.
44 A. Rodríguez-Fortea, P. Alemany, S. Alvarez and E. Ruiz, *Chem. – Eur. J.*, 2001, **7**, 627–637.
45 R. L. Carlin, *Magnetochemistry*, Springer Science & Business Media, 2012.
46 S. S.-Y. Chui, S. M.-F. Lo, J. P. Charmant, A. G. Orpen and I. D. Williams, *Science*, 1999, **283**, 1148–1150.
47 B. Moulton, J. Lu, R. Hajndl, S. Hariharan and M. J. Zaworotko, *Angew. Chem.*, 2002, **114**, 2945–2948.
48 S. Feng, H. Duan, H. Tan, F. Hu, C. Liu, Y. Wang, Z. Li, L. Cai, Y. Cao, C. Wang, Z. Qi, L. Song, X. Liu, Z. Sun and W. Yan, *Nat. Commun.*, 2023, **14**, 7063.
49 D. Maspoch, D. Ruiz-Molina and J. Veciana, *Chem. Soc. Rev.*, 2007, **36**, 770–818.
50 L. Shen, S.-W. Yang, S. Xiang, T. Liu, B. Zhao, M.-F. Ng, J. R. Göettlicher, J. Yi, S. Li and L. Wang, *J. Am. Chem. Soc.*, 2012, **134**, 17286–17290.
51 S. Shi, D. Gao, Q. Xu, Z. Yang and D. Xue, *CrystEngComm*, 2015, **17**, 2118–2122.
52 D. Gao, J. Zhang, J. Zhu, J. Qi, Z. Zhang, W. Sui, H. Shi and D. Xue, *Nanoscale Res. Lett.*, 2010, **5**, 769.
53 E. Wasserman, L. C. Snyder and W. A. Yager, *J. Chem. Phys.*, 1964, **41**, 1763–1772.
54 W. R. Hagen, *Int. J. Mol. Sci.*, 2023, **24**, 14793.
55 J. A. Weil and J. R. Bolton, *Electron paramagnetic resonance: elementary theory and practical applications*, John Wiley & Sons, 2007.
56 A. Ozarowski, *Inorg. Chem.*, 2008, **47**, 9760–9762.
57 A. Bencini and D. Gatteschi, *Electron paramagnetic resonance of exchange coupled systems*, Springer Science & Business Media, 2012.
58 P. K. Ross, M. D. Allendorf and E. I. Solomon, *J. Am. Chem. Soc.*, 1989, **111**, 4009–4021.
59 L. Gutierrez, G. Alzuet, J. Borrás, A. Castineiras, A. Rodríguez-Fortea and E. Ruiz, *Inorg. Chem.*, 2001, **40**, 3089–3096.
60 M. Perec, R. Baggio, R. P. Sartoris, R. C. Santana, O. Peña and R. Calvo, *Inorg. Chem.*, 2010, **49**, 695–703.
61 M. Simenas, M. Kobalz, M. Mendt, P. Eckold, H. Krautscheid, J. R. Banys and A. Pöppl, *J. Phys. Chem. C*, 2015, **119**, 4898–4907.
62 V. Paredes-García, R. C. Santana, R. Madrid, A. S. Vega, E. Spodine and D. Venegas-Yazigi, *Inorg. Chem.*, 2013, **52**, 8369–8377.
63 A. Pöppl, S. Kunz, D. Himsl and M. Hartmann, *J. Phys. Chem. C*, 2008, **112**, 2678–2684.
64 S. Reja, D. Sarkar, K. Sarkar, D. Mukherjee, T. Fayaz, P. Sanphui and R. K. Das, *Inorg. Chim. Acta*, 2024, **560**, 121809.
65 G. Borthagaray, M. Mondelli and M. Torre, *J. Infect. Dis. Epidemiol.*, 2016, **2**, 10.23937.
66 S. K. Nandanwar and H. J. Kim, *ChemistrySelect*, 2019, **4**, 1706–1721.
67 A. C. Hangan, R. L. Lucaciu, A. Turza, L. Dican, B. Sevastre, E. Páll, L. S. Oprean and G. Borodi, *Int. J. Mol. Sci.*, 2023, **24**, 13819.
68 J. A. Lemire, J. J. Harrison and R. J. Turner, *Nat. Rev. Microbiol.*, 2013, **11**, 371–384.
69 A. B. Abdelhadi, S. Rodríguez-Sánchez, R. Ouarsal, M. Saadi, L. El Ammari, N. Morley, B. El Bali, Ó. Gómez-Torres, M. Lachkar and A. Douhal, *Mater. Adv.*, 2024, **5**, 3058–3066.
70 T. BG, *Phytopathology*, 1964, **55**, 910–918.
71 C. Barbot, L. Gouriou, M. Mignot, M. Sebban, P. Zhang, D. Landy, C.-C. Ling and G. Gouhier, *Molecules*, 2025, **30**, 3263.
72 S. Arulmozhi, G. Sasikumar, A. Subramani, M. K. Mohammed, S. J. A. Ali, S. Ponnusamy, M. S. Jabir, A. M. Elgorban, W. Zhang and H. Natarajan, *ACS Omega*, 2023, **8**, 34458–34470.
73 D. Majumdar, J. E. Philip, S. Roy, B. Gassoumi and H. Ghalla, *BMC Chem.*, 2025, **19**, 227.
74 S. S. A. Fathima, M. M. S. Meeran and E. Nagarajan, *Struct. Chem.*, 2020, **31**, 521–539.
75 CCDC 2468965: Experimental Crystal Structure Determination, 2025, DOI: 10.5517/ccdc.csd.cc2nw51s.